

# Electrical conductivity of LSGM–YSZ composite materials synthesized via coprecipitation route

Raghvendra · Rajesh Kumar Singh · Prabhakar Singh

Received: 30 November 2013 / Accepted: 18 April 2014 / Published online: 13 May 2014  
© Springer Science+Business Media New York 2014

**Abstract** Composites of Strontium- and Magnesium-doped lanthanum gallate,  $\text{La}_{0.9}\text{Sr}_{0.1}\text{Ga}_{0.8}\text{Mg}_{0.2}\text{O}_{2.85}$  (LSGM), and yttria-stabilized zirconia,  $\text{Zr}_{0.9}\text{Y}_{0.1}\text{O}_{1.95}$  (YSZ), with weight ratios of 9.5:0.5, 9:1 and 8.5:1.5 were first prepared by co-precipitation route. The component compounds, LSGM and YSZ were also prepared by the same route for comparative study. X-ray Rietveld analyses revealed that the sintered LSGM–YSZ composites contain mainly perovskite orthorhombic LSGM phase along with fluorite YSZ phase similar to that of the cubic zirconia. Scanning Electron Microscopic image of the composite depicted the spherical- and oval-shaped grains. XPS spectra of the composite exhibited the LSGM along with a trace amount of the YSZ constituents. Electrical conductivity of the three systems was measured in the frequency range 20 Hz–1 MHz and in the temperature range of 400–700 °C. LSGM–YSZ composite electrolyte with 9:1 ratio was found to exhibit enhanced electrical conductivity in comparison to LSGM and YSZ systems. Moreover, it exhibited lower activation energy than that of their individual components.

## Introduction

Sr- and Mg-doped  $\text{LaGaO}_3$  perovskite has been proposed as a promising electrolyte material with good oxygen ionic conductivity at relatively low temperatures [1–4]. The oxygen ion conductivity of  $\text{La}_{1-x}\text{Sr}_x\text{Ga}_{1-y}\text{Mg}_y\text{O}_{3-\delta}$  (LSGM, with  $x = 0.1$  and  $y = 0.2$ ) has been reported to be around 0.10 S/cm at 800 °C, which is comparable to that of yttria-

stabilized zirconia (YSZ) at 1000 °C. Nevertheless, the doped  $\text{LaGaO}_3$  has been reported to show chemical instability with electrode materials, because of inter-diffusion of metal components at the interface between LSGM electrolyte and the perovskite cathode materials [5–7]. Composite electrolytes have been identified as interesting alternative electrolyte material bearing advantage of both the components in terms of conductivity and/or stability [8–12]. In 1973, Liang [8] reported a substantial increase in ionic conductivity of lithium iodide with incorporation of the inert phase, e.g. aluminium oxide. Mishima et al. [10] investigated the samarium-doped ceria (SDC)–YSZ composite electrolyte, and found that the addition of SDC demonstrates an improvement in the electrical conductivity of the composite electrolyte. Kim and co-authors [11] have also fabricated the composite electrolytes for low-temperature solid oxide fuel cells by coating YSZ sol on tape-casted substrates of yttria-doped ceria (YDC) and gadolinia-doped ceria (GDC). The results of single cell tests showed that YSZ layer-coated-doped ceria composite electrolyte, prepared by the sol–gel dip-drawing method, has a superior single cell performance in comparison to YSZ electrolyte without dissociation of ceria substrate. However, the YSZ and doped ceria composite may have the problem of inter-diffusion of components at the interfaces, causing a decrease in conductivity [13–15]. It is already reported that for the SDC–LSGM composite electrolyte system bears the highest ionic conductivity for weight ratio 9:1 [16]. Also, for LSGM–GDC composite system, the electrical conductivity was found to show the highest value again for weight ratio 9:1 [17]. Moreover, Li et al. [18] have shown the similar result for LSGM–SDC composite system for weight ratio 9:1. Nevertheless, Hao et al. [19] have mentioned that SDC–LSGM electrolyte exhibits maximum electrical conductivity and power density for weight ratio 9.5:0.5.

Raghvendra · R. K. Singh · P. Singh (✉)  
Department of Physics, Indian Institute of Technology (BHU),  
Varanasi 221005, India  
e-mail: psingh.app@iitbhu.ac.in

Since perovskite LSGM and Fluorite YSZ are reported as a very good oxide ion conductor, therefore, composite of these two can be synthesized. Looking at the majority of the results reported for other composite electrolyte materials, we synthesized and investigated the electrical properties of LSGM–YSZ composite material with weight ratios 9.5:0.5, 9:1 and 8.5:1.5. In this work, we have studied the phase formation, elemental confinement, electrical and thermal expansion properties of synthesized systems. Composites were prepared by co-precipitation method. LSGM and YSZ were also prepared and investigated for comparative study.

## Materials and methods

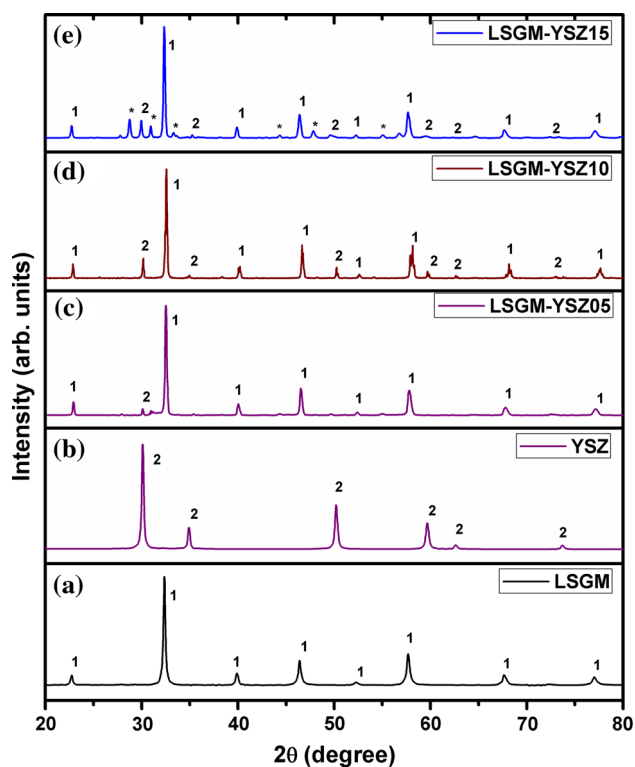
Co-precipitation method was used to prepare LSGM, YSZ and LSGM–YSZ composites. Stoichiometric amounts of high purity of constituent oxides were dissolved in nitric acid solution by stirring on a hot plate. After the complete dissolution of the component oxides, this solution was added drop wise into a stirred ammonia solution at 80 °C. White precipitate was formed at pH value around 9. The resulting precipitate was then kept for 24 h on a hot plate and was then evaporated in the oven at 160 °C. Calcination was subsequently carried out for the dry LSGM and YSZ precursors at 1250 °C for 12 h. LSGM–YSZ composites were prepared with a LSGM to YSZ weight ratio of 9.5:0.5, 9:1 and 8.5:1.5. All calcined powders were ground in an agate mortar, and then uniaxially pressed into pellets with a compaction load of  $\sim 100$  kg/cm<sup>2</sup>. The green pellets were sintered at 1400 °C for 12 h at the heating rate 4 °C/min, and then were allowed for furnace cooling.

X-ray diffraction patterns of the samples were examined using powder X-ray diffraction (XRD) (Rigaku, Miniflex II desktop) technique with Cu–K $\alpha$  radiation (30 kV, 20 mA) in the range of 20°–80°. SEM micrographs of these samples were recorded using Quanta 200 FESEM. A Kratos Analytical Axis Ultra XPS system was used to perform elemental and bonding state analysis. The residual vacuum in the analysis chamber was kept at  $10^{-5}$  Pa. The binding energy of C 1s (284.6 eV) was used as an internal standard. A monochromatic Al K $\alpha$  source operated at 15 kV and pass energy of 20 eV was used to obtain elemental core level spectra. For electrical measurement, the sintered pellets were first wet-ground to remove the surface layer. Then, High temperature Ag-paste was applied on both sides of the pellet and cured/fired at 750 °C for 1 h. Impedance measurements of these pellets were made from 400 to 700 °C at the intervals of 20 °C in the frequency range 20 Hz–1 MHz using Wayne Kerr (6500 P) impedance analyser. Dilatometry of the three systems was

performed in air using a dilatometer DIL 402 PC (NET-ZSCH, UK) from room temperature to 1000 °C.

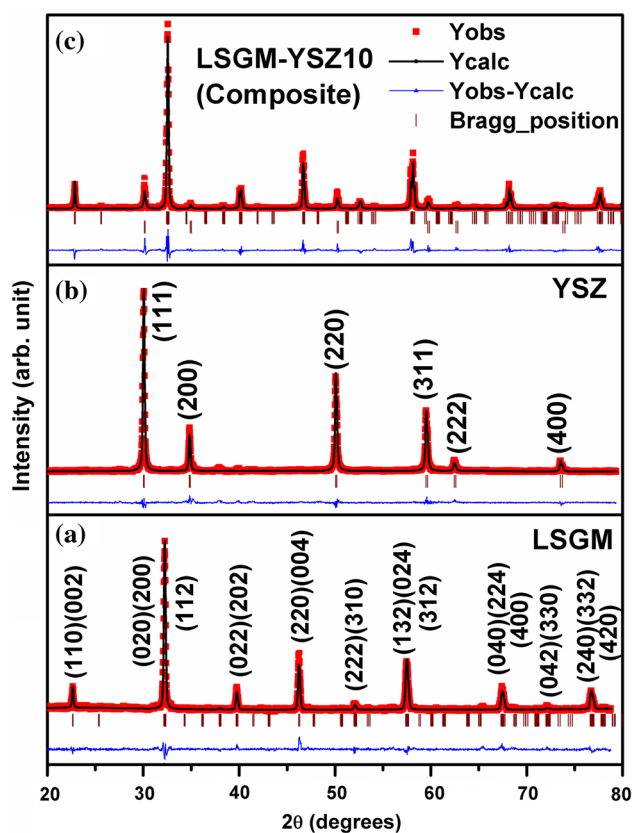
## Results and discussion

In present discussion, the system La<sub>0.9</sub>Sr<sub>0.1</sub>Ga<sub>0.8</sub>Mg<sub>0.2</sub>O<sub>3– $\delta$</sub>  is designated as LSGM, system Zr<sub>0.9</sub>Y<sub>0.1</sub>O<sub>1.95</sub> as YSZ and their composites with weight ratios 9.5:0.5, 9:1 and 8.5:1.5 are designated as LSGM–YSZ05, LSGM–YSZ10 and LSGM–YSZ15, respectively. Figure 1 shows the XRD patterns of all the synthesized systems viz. LSGM, YSZ and their composites. LSGM and YSZ phases are represented by the symbols 1 and 2 in the Fig. 1. These phases are also marked in their composites. A trace amount of the secondary phase of the La<sub>2</sub>Zr<sub>2</sub>O<sub>7</sub> (indicated by \* in the Fig. 1) is observed in the LSGM–YSZ15 composite [ICDD card No. 73-0444]. This phase is observed due to the reaction of the lanthanum with zirconia during the heat treatment of the aforementioned composite [20, 21]. This is an insulating phase, which reduces the electrical conductivity of the LSGM–YSZ15 system. In present investigation, we have obtained optimized conductivity for LSGM–YSZ10 system, therefore, the physical behaviour of this system along with its individual parent compositions (LSGM and YSZ) has been discussed. The X-ray Rietveld refined diffraction patterns of the sintered LSGM, YSZ and LSGM–YSZ10 composite are shown in Fig. 2(a), (b) and (c), respectively. The XRD patterns of LSGM and YSZ are also included as reference. To obtain the structural parameters, we have performed Rietveld analyses of the XRD data applying Fullprof program. The peak shape was assumed to be pseudo-Voigt functions. The background of each profile was approximated by a 6-parameter polynomial. It was found that the composite, after sintering at 1400 °C, consists perovskite orthorhombic LSGM as a major phase (space group, *Pnma*, 62) along with minor YSZ phase having structure similar to that of the cubic fluorite ZrO<sub>2</sub> phase (space group, *Fm*  $\bar{3}m$ , 225). Goodenough and Feng [2] reported that the La<sub>0.9</sub>Sr<sub>0.1</sub>Ga<sub>0.8</sub>Mg<sub>0.2</sub>O<sub>2.85</sub> (LSGM) phase as cubic perovskite, whilst Ishihara et al. [1] have reported an orthorhombic structure for this material. In this study, the powder patterns of LSGM were indexed using the orthorhombic cell and Rietveld refinements was carried out on this basis [22, 23]. The results of Rietveld full pattern refinement are shown in Fig. 2. The atomic model, which gives the best fit to the data for LSGM, was orthorhombic space group *Pnma* (no. 62) with refined cell dimensions as mentioned in Table 1. Prominent diffraction peaks of LSGM system are indexed with ICDD card no. 89-7946. X-ray Rietveld analysis of the zirconia system was performed assuming it as cubic phase and peaks are indexed with ICDD card no.



**Fig. 1** X-Ray diffraction patterns of **a** LSGM, **b** YSZ and **c** LSGM–YSZ05, **d** LSGM–YSZ10 and **e** LSGM–YSZ15 composites at room temperature. 1 and 2 represents the LSGM and YSZ phase, respectively. Asterisk correspond the secondary phase of  $\text{La}_2\text{Zr}_2\text{O}_7$  in LSGM–YSZ15 composite

89-9065. Rietveld analysis of the composite system was performed assuming a two-phase system (LSGM and YSZ). On the basis of Rietveld refinement process, we found  $\sim 89$  wt% of LSGM phase and  $\sim 11$  wt% of YSZ phase in the LSGM–YSZ10 composite. Table 1 enumerated the various structural parameters obtained from the Rietveld refinements of the three synthesized systems. The densities of the sintered samples were determined using Archimedes principle and for composite, it was found to be about 96 % of its theoretical density. SEM micrographs of the fractured surface of the sintered pellets were recorded for all the three systems. Figure 3 depicts the SEM micrograph of LSGM–YSZ10 composite. This figure shows spherical- and oval-shaped dense and well-connected grain and grainboundary morphology. Composite phases (LSGM and YSZ) are also indicated in this figure. X-ray photoelectron spectroscopy (XPS) spectra of LSGM, YSZ and the composite LSGM–YSZ10 are shown in Fig. 4. XPS studies were carried out on air-annealed samples in order to identify the bond character and chemical states constituents of LSGM, YSZ and composite. In LSGM and YSZ system, binding energy peaks may be attributed to their characteristic chemical states. The appearance of C 1s peak may originate from external

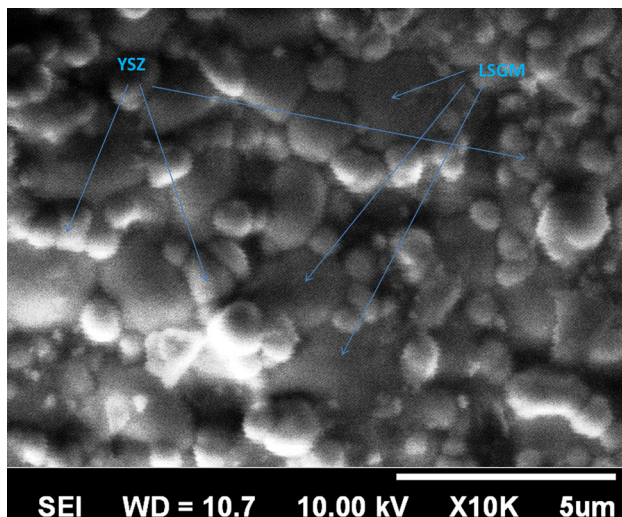


**Fig. 2** X-ray Rietveld refinement diffraction patterns fitting of **a** LSGM, **b** YSZ and **c** composite LSGM–YSZ10. Here *Yobs*, *Ycalc*, *Yobs–Ycalc* and *Bragg position* represent the experimental data, calculated data, the difference of experimental and calculated data and Bragg’s positions, respectively

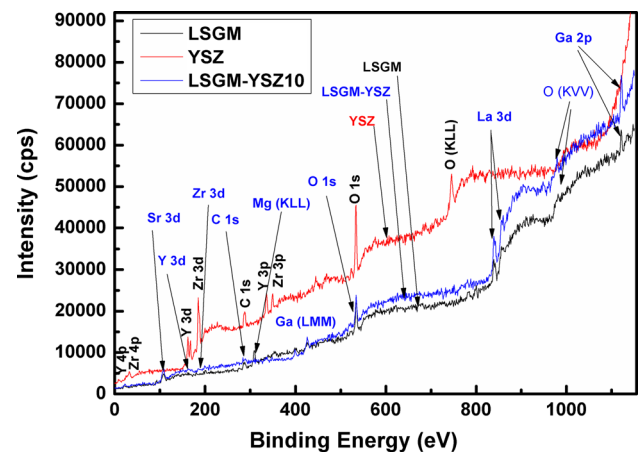
contamination. This is common to XPS spectra of any material. After calibration with respect to the C 1s reference peak at 284.6 eV, XPS analysis was performed for all the samples. In the survey of the XPS spectra of LSGM, La 3d, Sr 3d, Ga 2p, Mg 1s and O 1s were assigned at the characteristic peak positions. The binding energy peaks of La 3d, Sr 3d, Ga 2p and O1s have been observed at  $\sim 836$ ,  $\sim 135$ ,  $\sim 1117$  and  $\sim 530$  eV, respectively. These binding energy peaks also corroborate with earlier reported literature [24, 25]. In YSZ system, the binding energy peaks of Y  $3d_{5/2}$  and Zr  $3d_{5/2}$  were found to appear at  $\sim 157.4$  and  $\sim 182.1$  eV, respectively. This agrees well with published values for Y  $3d_{5/2}$  at 157.2–158.6 eV and Zr  $3d_{5/2}$  at 182.2–184.0 eV [26]. The XPS spectra of the composite LSGM–YSZ10 show the presence of constituent element of both systems. The XPS spectra of the composite material indicate very low relative intensity peaks of the YSZ constituents and relatively high intensity peaks of the LSGM constituents. This confirms the presence of a trace amount of the YSZ and major amount of LSGM in the composite system of the LSGM–YSZ10.

**Table 1** Parameters obtained from the Rietveld refinement of the XRD data for the LSGM, YSZ and LSGM–YSZ10 composite system

System	Lattice parameters	Atoms	Wyckoff positions	Fractional position co-ordinates			“R” values		
				x	y	z	R <sub>p</sub>	R <sub>wp</sub>	χ <sup>2</sup>
LSGM	a = 5.5424 (5)	La (Sr)	4c	0.005 (5)	0.25 (6)	−0.0017 (4)	9.12	12.8	4.16
	b = 7.8502 (9)	Ga (Mg)	4b	0	0	0.5			
	c = 5.5602 (6)	O (O1)	4c	−0.027 (2)	0.25 (5)	0.433 (8)			
		O (O2)	8d	0.256 (9)	0.460 (3)	−0.267 (5)			
YSZ	a = 5.1481 (8)	Zr (Y)	4a	0	0	0	9.78	13.5	3.82
		O	8c	0.25	0.25	0.25			
Composite (LSGM–YSZ10)	LSGM phase	La (Sr)	4c	0.015 (9)	0.250 (6)	−0.0027 (7)	10.4	14.4	4.96
	a = 5.5176 (8)	Ga (Mg)	4b	0	0	0.5			
	b = 7.7681 (6)	O (O1)	4c	−0.047 (9)	0.25	0.543 (8)			
	c = 5.4863 (3)	O (O2)	8d	0.266 (7)	0.480 (3)	−0.284 (5)			
	YSZ phase	Zr (Y)	4a	0	0	0			
	a = 5.1584 (9)	O	8c	0.25	0.25	0.25			

**Fig. 3** SEM image of the sintered polished surface of LSGM–YSZ10 composite

Real part of the frequency-dependent electrical conductivity of the three studied systems is shown in Fig. 5(a), (b) and (c), at a few temperatures. Any polycrystalline ceramic material comprises the contributions of the grain, grain-boundary and the electrode-specimen interface to the total electrical conductivity. In Fig. 5, the low-frequency plateau represents the total conductivity (the DC conductivity,  $\sigma_{dc}$ ) of the sample followed by a dispersion region (AC conductivity,  $\sigma_{ac}$ ) caused by the combined effect of grain conductivity and grainboundary relaxation processes [27]. Clearly, Fig. 5 reveals that conductivity isotherms of these systems consist of two parts viz. a frequency-independent part in the low-frequency regime (DC conductivity,  $\sigma_{dc}$ ) and frequency-dependent dispersion part (AC conductivity,  $\sigma_{ac}$ ) in

**Fig. 4** XPS spectra of LSGM, YSZ and LSGM–YSZ10 composite

the high-frequency regime. The DC conductivity is caused by the random hopping motion of the ions among the crystal defects, and the AC conductivity is caused by the correlated forward–backward hopping of the ions among the localized sites [28]. The DC conductivity can be evaluated by extrapolating the low-frequency plateau. Nevertheless, the real part of the electrical conductivity of the system can be written as

$$\sigma' = \sigma_{dc} + \sigma_{ac}, \quad (1)$$

where the ac conductivity,  $\sigma_{ac}$ , can be, in general, given as  $\sigma_{ac}(\nu, T) = A(T) \cdot \nu^p$  [28, 29]. Here factor  $A$  depends on several parameters like absolute temperature, number of vacant sites in the material and the average hopping length between randomly distributed localized sites. Equation (1) can be rearranged as

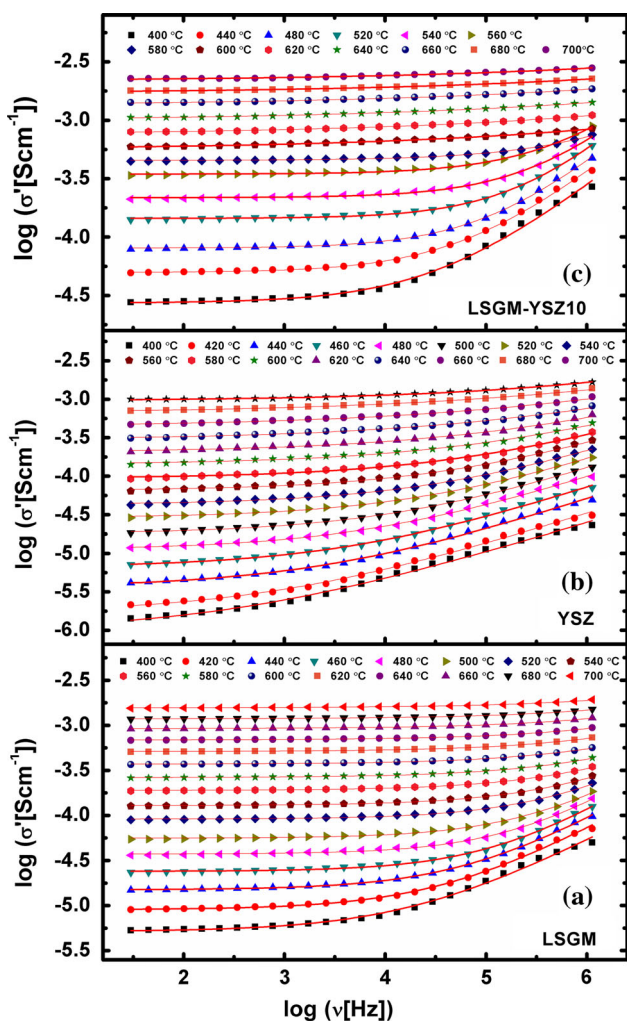


Fig. 5 Frequency-dependent conductivity spectra of the LSGM, YSZ and LSGM–YSZ10 composite

$$\sigma' = \sigma_{dc} \left[ 1 + \frac{\sigma_{ac}}{\sigma_{dc}} \right] \text{ or } \sigma' = \sigma_{dc} \left[ 1 + \frac{A\nu^p}{\sigma_{dc}} \right],$$

$$\text{or } \sigma' = \sigma_{dc} \left[ 1 + \left( \frac{\nu}{\nu_H} \right)^p \right] \text{ with } \nu_H = \left( \frac{\sigma_{dc}}{A} \right)^{1/p}, \quad (2)$$

where  $\nu_H$  is the hopping frequency,  $\nu$  is the frequency and exponent  $p$  is usually found to be less than unity. Equation 2 is the Almond and West formulation of Jonscher power law [30–32].

The conductivity spectra for the three systems are described using Eq. (2). The solid line in Fig. 4 shows the fitting to the data points using Eq. (1). A very good fitting with error less than 2 % is obtained in present investigation. The DC conductivity,  $\sigma_{dc}$ , and the hopping angular frequency (hopping rate),  $\omega_H$ , were obtained from the fitting parameters.

The activation energies of conductivity and hopping frequency for all three systems were calculated from the Arrhenius equations given as

$$\sigma_{dc} \cdot T = \sigma_o \exp(-E_a/kT) \quad (3)$$

and

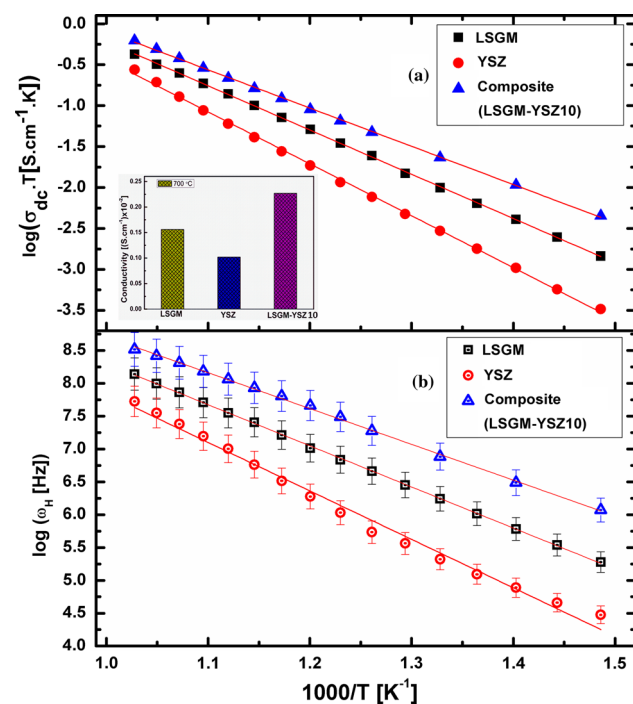
$$\omega_H = \omega_e \exp(-E_\omega/kT), \quad (4)$$

where  $\sigma_{dc}$  is the electrical conductivity,  $\sigma_o$  is pre-exponential factor,  $E_a$  is activation energy for conduction,  $k$  is Boltzmann constant,  $T$  is the absolute temperature,  $\omega_e$  is the effective attempt frequency introduced by the true attempt frequency ( $\omega_0$ ) and with the enhancement produced by a finite entropy of migration and  $E_\omega$  is the activation energies for migration. [33, 34]. The activation energies for conduction of the three investigated systems are mentioned in Table 2. Arrhenius representation of DC conductivity and the ion hopping rate, calculated from Eq. (2), for LSGM, YSZ and LSGM–YSZ10 composite are depicted in Fig. 6(a) and (b), respectively. The hopping rate shown in Fig. 6(b) includes error bars as the evaluation of this parameter depends on the frequency range in which the dispersive regime is available formally known as ‘window effect’ [35, 36]. Both DC conductivity and hopping frequency show almost identical behaviour, with a linear region in the investigated temperature range. The activation energies for conduction,  $E_a$  and migration ( $E_\omega$ ) were almost identical to that of the activation energy of the DC conductivity ( $E_a$ ). Moreover, the trend of variation of  $E_\omega$  was observed to be almost similar to that of the  $E_a$ . The power law dependence of the DC conductivity and ion hopping rate is also reported in the various literatures [33, 34, 37]. The values of activation energy obtained for YSZ and LSGM corroborate with the earlier reported values [2, 3]. From the Table 2, it can be seen that the activation energy for conduction of LSGM–YSZ composite electrolyte is lower than that of the LSGM and YSZ. This reveals that the electrical conduction of the composite electrolyte has lower energy barrier than that of the two components. From Fig. 6(a), it can be seen that the LSGM–YSZ composite exhibits the highest conductivity in the measured temperature range. DC conductivity at 700 °C for all the samples is mentioned in Table 2.

The electrical properties of two-phase system can be understood in terms of defect chemistry. Interfaces play an important role for the transport properties of polycrystalline and polyphase (composite) materials. It is generally accepted that the space charge layer exists in the two-phase system [9, 38, 39]. The inter-diffusion and reaction rate depend strongly on the powder morphology. The co-precipitation method produces fine particles and an intimate mix of the component oxides. This leads to a large contacting interface between LSGM and YSZ. Jiang and Wagner [40] have proposed that for composite electrolytes,

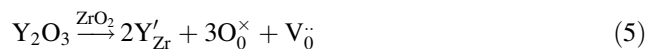
**Table 2** Structural and electrical parameters of LSGM, YSZ and LSGM–YSZ composites

Composition	Average crystallite size (nm)	Relative density	Conductivity (at 700 °C) $\Omega^{-1} \text{cm}^{-1}$	Activation energy ( $E_{\sigma}$ ) (eV)
LSGM	44	96.8 %	$0.156 \times 10^{-2}$	1.06
YSZ	39	95.2 %	$0.102 \times 10^{-2}$	1.21
LSGM–YSZ05	36	96.7 %	$0.219 \times 10^{-2}$	0.99
LSGM–YSZ10	38	96.3 %	$0.227 \times 10^{-2}$	0.93
LSGM–YSZ15	41	96.1 %	$0.198 \times 10^{-2}$	0.92

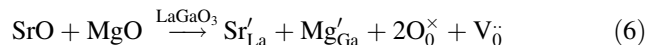
**Fig. 6** Arrhenius representation of **a** DC conductivity and **b** the hopping rate of LSGM, YSZ and LSGM–YSZ10 composite

the space charge is originated from the formation of a thin amorphous phase by defect reaction at the interface between the second phase and the matrix. They also mentioned that the enhancement of the density of the mobile ionic defects takes place in the space charge region. The different mobile charge carriers can be generated in the present systems as explained below.

The incorporation of yttria into the zirconia stabilizes the cubic fluorite phase and creates the oxygen ion vacancies, and hence increases the electrical conductivity. The existence of vacancies on the oxygen site causes high ionic conductivity in YSZ. The oxygen ions are transported by hopping through these vacant sites [6]. This can be written by the following defect equation



$\text{LaGaO}_3$  is the base compound in which La and Ga sites can be doped with divalent ions. When  $\text{Sr}^{2+}$  and  $\text{Mg}^{2+}$  are doped at La and Sr site of  $\text{LaGaO}_3$ ; oxygen vacancies are formed according to the following defect reactions [25].



Kröger–Vink notions have been adopted to write the above defect equation. The activation energy normally includes the formation energy and the migration energy of the oxygen vacancies. Knauth [39] proposed that the point defects and the dopants interact with interfaces. These defects can be trapped at the interface cores. The accumulation of charges in the space charge regions leads to an enhancement of the electrical conductivity. In the composite of LSGM and YSZ, both the defect mechanisms (generated by Eqs. 5 and 6) are responsible for the generation of the defects interacting with the interfaces. This results into an enhanced electrical conductivity in the composite system in comparison to the individual components.

In order to understand our findings of electrical conductivity of the investigated systems, we have analysed the conductivity data in terms of impedance plots also. The impedance spectrum generally separates grain (bulk), grainboundary and electrode processes of the ceramics [41]. It is well known that the semicircle at low-frequency regimes represents grainboundary contribution and the semicircle at higher frequencies represents contribution of grain (bulk) conductivity to the total conductivity. Figure 7 shows the Nyquist plot (cole–cole plot) of the sintered specimens at 500 °C. This figure clearly reveals the presence of two semicircles, however, the boundary of the two semicircles is not well separated and it is almost merged. This indicates that grain and grainboundary relaxations take place simultaneously at the common boundary of the two semicircles. The intercepts of the semicircles on real axis (on  $Z'$ -axis) represent the corresponding grain (bulk) and grainboundary conductivities in high- and low-frequency regimes, respectively. The inset of Fig. 7 shows the Cole–Cole plot of the composite at a few temperatures. Figure 7 clearly reveals that LSGM–YSZ10 composite has the lowest total resistance (highest conductivity) in comparison to LSGM and YSZ. This may be due to the space charge layer formed at the phase interfaces. It is generally accepted that the space charge layer exists in the two-phase system [42]. The enhancement of the concentration of vacancies or interstitials is expected at the space charge region which is more likely to form at the interfaces of the grainboundary [43]. In other words, the mobile charges in the composite electrolyte may exist along grain boundaries,

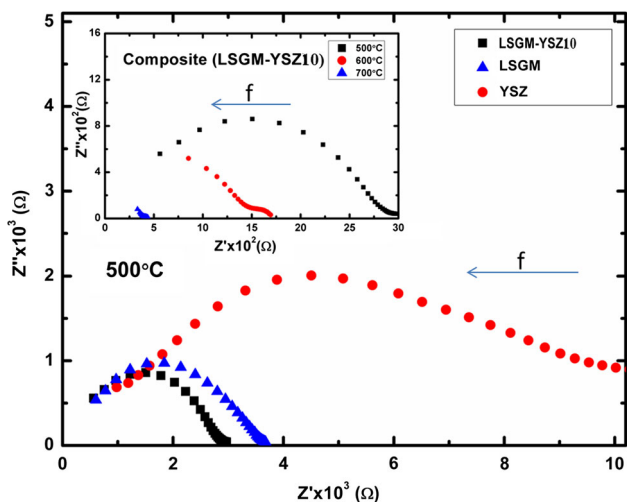


**Fig. 7** Nyquist impedance plot of the LSGM, YSZ and LSGM-YSZ10 composite at 500 °C. Inset depicts the Cole–Cole representation of the composite at a few temperatures

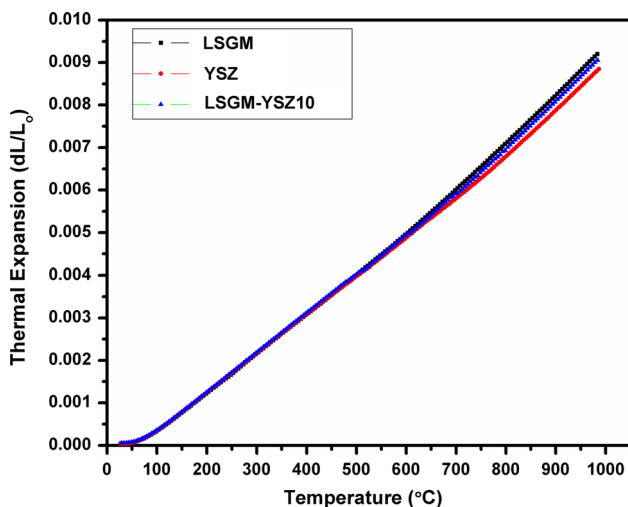


**Fig. 8** Thermal expansion curves for the LSGM, YSZ and LSGM-YSZ10 composite samples sintered at 1400 °C for 12 h

and thus provides a space charge layer at the interfaces. Therefore, LSGM–YSZ composite electrolyte, in present case, exhibits enhanced electrical conductivity in comparison to its individual components. Thus, LSGM–YSZ10 composite material could be a promising electrolyte material for SOFC system.

Figure 8 shows the linear thermal expansion plots of the LSGM, YSZ and LSGM–YSZ10 composite samples sintered at 1400 °C for 12 h. It can be seen that thermal expansion coefficients are very close before reaching 500 °C. As the temperature is increased above 500 °C, the thermal expansion coefficient of the LSGM sample becomes gradually higher than that of the YSZ sample. The thermal expansion coefficient of the LSGM is somewhat higher than that of the YSZ. Nevertheless, the TEC value of the

composite (LSGM–YSZ10) is slightly less than LSGM but higher than that of the YSZ at higher temperature regime [44]. The average thermal expansion coefficients of the LSGM, YSZ and LSGM–YSZ10 samples were found to be  $10.1 \times 10^{-6}$ ,  $9.73 \times 10^{-6}$  and  $9.98 \times 10^{-6}/^{\circ}\text{C}$ , respectively, in the temperature range 30–1000 °C [44].

### Conclusions

The structural and electrical properties of LSGM–YSZ composite in weight ratios 9.5:0.5, 9:1 and 8.5:1.5 were investigated along with the individual components LSGM and YSZ. Composites of LSGM–YSZ contain LSGM orthorhombic perovskite as a major phase and YSZ cubic fluorite as a minor phase. The XPS spectra also confirm the findings of XRD result. SEM micrograph also depicts the existence of both the phases in the composite system. Conductivity spectra were found to follow Jonscher Power Law behaviour and found to consist of two parts the frequency-independent (DC conductivity) and frequency-dependent parts (AC conductivity). An improved electrical conductivity was obtained in the composite system (LSGM–YSZ10) in comparison to that of the two individual components. The space charge layers, formed at the interface between the two phases (LSGM and YSZ), were found to be responsible for the enhanced electrical conductivity in the LSGM–YSZ10 composite system in the temperature range 400–700 °C. The conduction behaviour was also understood in terms of impedance plot. The total conductivity was found to show the similar behaviour to that of obtained from the analysis of conductivity spectra. The enhanced conductivity of LSGM–YSZ10 composite indicates that the composite processing could be a promising method for improvement in electrical conductivity of the electrolyte for SOFC.

**Acknowledgements** We acknowledge DST-SERC for funding this work through its project sanction letter No. SR/FTP/ETA-0005/2010. We are thankful to Prof. ASK Sinha and Prof. O.P. Pandey for providing XPS and TEC measurement facility, respectively. Mr. Raghendra is grateful to MHRD for providing teaching assistantship.

### References

1. Ishihara T, Matsuda H, Takita Y (1994) Doped LaGaO<sub>3</sub> perovskite type oxide as a new oxide ionic conductor. *J Am Chem Soc* 116:3801–3803
2. Feng M, Goodenough JB (1994) A superior oxide-ion electrolyte. *Eur J Solid State Inorg Chem* 31:663–669
3. Huang P, Petric A (1996) Superior oxygen ion conductivity of lanthanum gallate doped with strontium and magnesium. *J Electrochem Soc* 143:1644–1648
4. Cristiani C, Zampori L, Latorrata S, Pelosato R, Dotelli G, Ruffo R (2009) Carbonate coprecipitation synthesis of Sr- and Mg-doped LaGaO<sub>3</sub>. *Mater Lett* 63:1892–1894

5. Chen WX, Nie HW, Huang WH, Zheng R, Tu HY, Wen TL (2003)  $\text{La}_{0.6}\text{Sr}_{0.4}\text{Co}_{0.8}\text{Mn}_{0.2}\text{O}_{3-\delta}$  cathode for an intermediate temperature SOFC. *J Mater Sci Lett* 22:651–653
6. Shaula AL, Kharton VV, Marques FMB (2004) Phase interaction and oxygen transport in  $\text{La}_{0.8}\text{Sr}_{0.2}\text{Fe}_{0.8}\text{Co}_{0.2}\text{O}_{3-\delta}$ – $(\text{La}_{0.9}\text{Sr}_{0.1})_{0.98}\text{Ga}_{0.8}\text{Mg}_{0.2}\text{O}_3$  composites. *J Eur Ceram Soc* 24:2631–2639
7. Sakai N, Horita T, Yamaji K, Brito ME, Yokokawa H, Kawakami A, Matsuoka S, Watanabe N, Ueno A (2006) Interface stability among solid oxide fuel cell materials with perovskite structures. *J Electrochem Soc* 153:A621–A625
8. Liang CC (1973) Conduction characteristics of the lithium iodide-aluminium oxide solid electrolytes. *J Electrochem Soc* 120:1289–1292
9. Maier J (1985) Space charge regions in solid two-phase systems and their conduction contribution—I. Conductance enhancement in the system ionic conductor–‘inert’ phase and application on  $\text{AgCl}:\text{Al}_2\text{O}_3$  and  $\text{AgCl}:\text{SiO}_2$ . *J Phys Chem Solids* 46:309–320
10. Mishima Y, Mitsuyasu H, Ohtaki M, Eguchi K (1998) Solid oxide fuel cell with composite electrolyte consisting of samaria-doped ceria and yttria-stabilized zirconia. *J Electrochem Soc* 145:1004–1007
11. Jang WS, Hyun SH, Kim SG (2002) Preparation of YSZ/YDC and YSZ/GDC composite electrolytes by the tape casting and sol–gel dip-drawing coating method for low-temperature SOFC. *J Mater Sci* 37:2535–2541. doi:10.1023/A:1015451910081
12. Wei B, Lü Z, Huang X, Li S, Ai G, Liu Z, Su W (2006) Electrochemical characteristics of  $\text{Ba}_{0.5}\text{Sr}_{0.5}\text{Co}_{0.8}\text{Fe}_{0.2}\text{O}_{3-\delta}$ – $\text{Sm}_{0.2}\text{Ce}_{0.8}\text{O}_{1.9}$  composite materials for low-temperature solid oxide fuel cell cathodes. *Mater Lett* 60:3642–3646
13. Hui S, Roller J, Yick S, Zhang X, Deces-Petit C, Xie Y, Maric R, Ghosh D (2007) A brief review of the ionic conductivity enhancement for selected oxide electrolytes. *J Power Sources* 172:493–502
14. Zhou XD, Scarfino B, Anderson HU (2004) Electrical conductivity and stability of CGO–YSZ solid solutions. *Solid State Ion* 175:19–22
15. Lee JH, Yoon SM, Kim BK, Lee HW, Song HS (2002) Electrical conductivity and defect structure of  $\text{CeO}_2$ – $\text{ZrO}_2$  mixed oxide. *J Mater Sci* 37:1165–1171. doi:10.1023/A:101436304942
16. Xu D, Liu X, Wang D, Yi G, Gao Y, Zhang D, Su W (2007) Fabrication and characterization of SDC–LSGM composite electrolytes material in IT-SOFC. *J Alloys Compd* 429:292–295
17. Jo SH, Muralidharan P, Kim DK (2010) Electrical conductivity studies on the LSGM–CGO composite electrolytes. *J Alloys Compd* 491:416–419
18. Li S, Li Z, Bergman B (2010) Lanthanum gallate and ceria composite as electrolyte for solid oxide fuel cells. *J Alloys Compd* 492:392–395
19. Hao G, Liu X, Wang H, Be H, Pei L, Su W (2012) Performance of  $\text{Ce}_{0.85}\text{Sm}_{0.15}\text{O}_{1.9}$ – $\text{La}_{0.9}\text{Sr}_{0.1}\text{Ga}_{0.8}\text{Mg}_{0.2}\text{O}_{2.85}$  composite electrolytes for intermediate-temperature solid oxide fuel cells. *Solid State Ion* 225:81–84
20. Liu YL, Hagen A, Barfod R, Chen M, Wang HJ, Poulsen FW, Hendriksen PV (2009) Microstructural studies on degradation of interface between LSM–YSZ cathode and YSZ electrolyte in SOFCs. *Solid State Ion* 180:1298–1304
21. Yang CCT, Wei WCJ, Roosen A (2004) Reaction kinetics and mechanisms between  $\text{La}_{0.65}\text{Sr}_{0.3}\text{MnO}_3$  and 8 mol% Ytria-stabilized zirconia. *J Am Ceram Soc* 87:1110–1116
22. Drennan J, Zelizk V, Hay D, Ciacchi FT, Rajendran S, Badwal SPS (1997) Characterisation, conductivity and mechanical properties of the oxygen-ion conductor  $\text{La}_{0.9}\text{Sr}_{0.1}\text{Ga}_{0.8}\text{Mg}_{0.2}\text{O}_{3-\delta}$ . *J Mater Chem* 7:79–83
23. Vasylechko L et al (2003) Crystal structure, thermal expansion and conductivity of anisotropic  $\text{La}_{1-x}\text{Sr}_x\text{Ga}_{1-2x}\text{Mg}_{2x}\text{O}_{3-y}$  ( $x = 0.05; 0.1$ ) single crystals. *J Solid State Chem* 172:396–441
24. Shkerin SN, Kuznetsov MV, Kalashnikova NA (2003) X-ray Photoelectron Spectroscopy of the Surface of Solid Electrolyte  $\text{La}_{0.88}\text{Sr}_{0.12}\text{Ga}_{0.82}\text{Mg}_{0.18}\text{O}_{3-x}$ . *Russ J Electrochem* 39:591–599
25. Raghvendra, Singh RK, Singh P (2014) Synthesis of  $\text{La}_{0.9}\text{Sr}_{0.1}\text{Ga}_{0.8}\text{Mg}_{0.2}\text{O}_{3-\delta}$  electrolyte via ethylene glycol route and its characterizations for IT-SOFC. *Ceram Int* 40:7177–7184
26. Jiang Y, Gao J, Liu M, Wang Y, Meng G (2007) Fabrication and characterization of  $\text{Y}_2\text{O}_3$  stabilized  $\text{ZrO}_2$  films deposited with aerosol-assisted MOCVD. *Solid State Ion* 177:3405
27. Waser R (1991) Bulk conductivity and defect chemistry of acceptor-doped strontium titanate in the quenched state. *J Am Ceram Soc* 74:1934–1940
28. Elliot SR (1987) AC conduction in amorphous-chalcogenide and pnictide semiconductors. *Adv Phys* 36:135–217
29. Singh P, Raghvendra, Parkash O, Kumar D (2011) Scaling of low-temperature conductivity spectra of  $\text{BaSn}_{1-x}\text{Nb}_x\text{O}_3$  ( $x \leq 0.100$ ): temperature and compositional-independent conductivity. *Phys Rev B* 84:174306–174312
30. Jonscher AK (1977) The ‘universal’ dielectric response. *Nature* 267:673–679
31. Jonscher AK (1983) Dielectric relaxation in solids. Chelsea Dielectric Press, London
32. Almond DP, West AR (1983) Anomalous conductivity prefactors in fast ion conductors. *Nature* 306:456–457
33. Almond DP, Duncan GK, West AR (1983) The determination of hopping rates and carrier concentrations in ionic conductors by a new analysis of ac conductivity. *Solid State Ion* 8:159–164
34. Almond DP, West AR (1983) Mobile ion concentrations in solid electrolytes from an analysis of A.C. conductivity. *Solid State Ion* 9&10:277–282
35. Sidebottom DL (1999) Ionic conductivity in glasses: is the window effect statistically relevant? *J Non Cryst Solids* 244:223–231
36. Singh P, Singh BP, Raghvendra (2012) Dispersion in AC conductivity of fragile glass melts near glass transition temperature. *Solid State Ion* 227:39–45
37. Almond DP, West AR (1987) The activation entropy for transport in ionic conductors. *Solid State Ion* 23:27–35
38. Maier J (1986) On the conductivity of polycrystalline materials. *Ber Bunsenges Phys Chem* 90:26–33
39. Knauth P (2000) Ionic conductor composites: theory and materials. *J Electroceram* 5:111–125
40. Jiang S, Wagner JB Jr (1995) A theoretical model for composite electrolytes—I. space charge layer as a cause for charge-carrier enhancement. *J Phys Chem Solids* 56:1101–1111
41. Macdonald JR (1987) Impedance spectroscopy: emphasizing solid materials and systems. Wiley Co., New York
42. Joshi AV, Wagner JRJB (1975) Electrochemical studies on single crystalline  $\text{CuCl}$  solid electrolyte. *J Electrochem Soc* 122:1071–1080
43. Fabbri E, Pergolesi D, Traversa E (2010) Ionic conductivity in oxide heterostructures: the role of interfaces. *Sci Technol Adv Mater* 11:054503–054512
44. Tietz F (1999) Thermal expansion of SOFC materials. *Ionics* 5:129–139